

Effects of Heteroatom Substitutions on the Crystal Structure, Film Formation, and Optoelectronic Properties of Diketopyrrolopyrrole-Based Materials

Jianhua Liu, Bright Walker, Arnold Tamayo, Yuan Zhang, and Thuc-Quyen Nguyen*

Substitution of the heteroatoms in the aromatic end-groups of three diketopyrrolopyrrole containing small molecules is investigated to evaluate how such substitutions affect various physical properties, charge transport, and the performance in bulk heterojunction solar cells. While the optical absorption and frontier orbital energy levels are insensitive to heteroatom substitution, the materials' solubility, thermal properties, film morphology, charge carrier mobility, and photovoltaic performance are altered significantly. Differences in material properties are found to arise from changes in intra- and intermolecular interactions in the solid state caused by heteroatom substitution, as revealed by the single crystal structures of three compounds. This study demonstrates a systematic investigation of structure–property relationships in conjugated small molecules.

1. Introduction

Conjugated molecules with different chemical structures have been widely reported and investigated as molecular donor materials in solution-processed bulk heterojunction (BHJ) solar cells.^[1–5] These conjugated molecules have a molecular architecture containing a conjugated backbone to achieve desired optoelectronic properties and alkyl side chains to enable solution processability. To efficiently absorb solar irradiation, the conjugated backbone usually incorporates chromophoric moieties such as benzoporphyrin,^[6] diketopyrrolopyrrole (DPP),^[7–11] isoindigo,^[12,13] squaraine,^[14–18] oligothiophene,^[19–23] borondipyrromethene,^[24,25] and merocyanine.^[26–28] The conjugation of the backbone is typically extended over several aryl moieties and ended by groups such as vinyl, thienyl, and phenyl derivatives.^[3,4] Given the vast combinations of different conjugated

moieties, detailed knowledge of how specific chemical moieties and structures translate to material properties remains limited. For example, the end functional groups are demonstrated to have a significant effect on material's photovoltaic properties in different molecular architectures such as oligothiophene,^[20,22] merocyanine,^[26,28] and DPP^[10,29] conjugated molecules. Understanding the effects that specific chemical moieties have on material and device properties is thus essential to facilitate the development of high performing materials.

In this work, we examine the effects of changing heteroatom substitutions in the aromatic end-groups of three

DPP-based materials (Figure 1): 3,6-bis(5-(benzofuran-2-yl)thiophen-2-yl)-2,5-bis(2-ethylhexyl)pyrrolo[3,4-c]pyrrole-1,4-dione (DPP(TBFu)₂),^[7] 3,6-bis(5-(benzothiophene-2-yl)thiophen-2-yl)-2,5-bis(2-ethylhexyl)pyrrolo[3,4-c]pyrrole-1,4-dione (DPP(TBTh)₂) and 3,6-bis(5-(indole-2-yl)thiophen-2-yl)-2,5-bis(2-ethylhexyl)pyrrolo[3,4-c]pyrrole-1,4-dione (DPP(TInd)₂). We find that the optical absorption and frontier orbital energy levels of the three compounds are less dependent on the heteroatom substitutions, while their thermal properties, solubility, crystallinity, film morphology, charge carrier mobility, and solar cell performance are significantly affected by the heteroatom substitutions in the end-conjugated units. Single crystal structures of the three compounds indicate that the effects of heteroatom substitutions are ascribed to changes in intra- and intermolecular interactions in the solid state caused by the heteroatom substitutions. Density functional theory (DFT) calculations are used to understand how heteroatom substitutions affect optical absorption and molecular conformation. These results provide insight into the effects of heteroatom substitution on the solid state and optoelectronic properties of conjugated molecules used in solution-processed organic solar cells.

2. Results and Discussions

The molecular structures of three DPP-containing compounds are shown in Figure 1. DPP(TBFu)₂ was synthesized according to the previously reported procedure;^[7] DPP(TBTh)₂ and DPP(TInd)₂ were successfully synthesized using a similar procedure (Supporting Information). DPP(TBFu)₂ and

Dr. J. Liu, Dr. B. Walker,^[+] Dr. A. Tamayo,^[++]
Dr. Y. Zhang, Prof. T.-Q. Nguyen
Center for Polymers and Organic Solids
Department of Chemistry and Biochemistry
University of California Santa Barbara
Santa Barbara, CA 93106, USA
E-mail: quyen@chem.ucsb.edu



[+] Present address: Interdisciplinary School of Green Energy, Ulsan National Institute of Science and Technology, Ulsan 689–798, Republic of Korea

[++] Present address: Next Energy Technologies, 5385 Hollister Avenue, Santa Barbara, CA 93111, USA

DOI: 10.1002/adfm.201201599

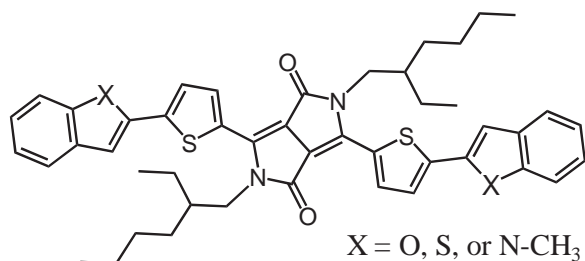


Figure 1. Chemical structures of three DPP derivatives with different ending heterocycles. $X = O$ for **DPP(TBFu)₂**, $X = S$ for **DPP(TBTh)₂**, and $X = N\text{-CH}_3$ for **DPP(TInd)₂**.

DPP(TBTh)₂ differ structurally only in the use of an oxygen or sulfur heteroatom respectively in the end-capping indene structure. In addition to using a nitrogen heteroatom, **DPP(TInd)₂** has *N*-methyl substitutions in the same indene structure. The structural variations among the three compounds ensure an effective investigation of the effects of heteroatom substitutions in the end-conjugated units.

2.1. Single Crystal Structures

Single crystal structures of three DPP derivatives were examined to investigate the effects of heteroatom substitution on the molecules' packing in the solid state. One advantage of conjugated molecules compared with conjugated polymers is that crystal structures can be solved via X-ray diffraction (XRD) when suitable single crystals are available. The single crystals of **DPP(TBFu)₂** and **DPP(TBTh)₂** were obtained by slow cooling saturated solutions in a chloroform and acetone mixture; the single crystal of **DPP(TInd)₂** was obtained in pure acetone using the same method.^[30] The crystallographic data is summarized in **Table 1**. All three compounds have different unit cell parameters and crystal morphology. **DPP(TBFu)₂** and **DPP(TBTh)₂** share a common crystal system (monoclinic) while **DPP(TInd)₂** exhibits a triclinic system. Optical images of these single crystals used for XRD analysis are displayed in Figure S1 (Supporting Information). **DPP(TBFu)₂** exhibits a needle-like crystal morphology while **DPP(TBTh)₂** and **DPP(TInd)₂** form a plate-like morphology. Crystallographic information files (CIFs) are provided in the Supporting Information.

Table 1. Crystallographic data for three DPP-containing conjugated molecules.

Compound	DPP(TBFu)₂	DPP(TBTh)₂	DPP(TInd)₂
Empirical formula	$C_{46}H_{48}N_2O_4S_2$	$C_{46}H_{48}N_2O_2S_4$	$C_{48}H_{54}N_4O_2S_2$
Morphology	Needle	Plate	Plate
Crystal system	Monoclinic	Monoclinic	Triclinic
Space group	P2/c	P2 ₁ /c	P-1
a (Å)	14.181(6)	5.966(1)	6.312(3)
b (Å)	5.165(2)	22.959(3)	12.336(7)
c (Å)	26.304(12)	14.324(2)	13.651(8)
α (°)	90	90	72.017(18)
β (°)	91.393(6)	98.239(6)	87.371(19)
γ (°)	90	90	80.701(18)
Z	2	2	1
R factor	3.88	9.49	12.41

It is known that the single crystal structure can differ from that in the film state due to possible crystal polymorphism. This can be evaluated by comparing the experimental annealed thin film XRD with theoretical patterns calculated from single crystal structures. **Figure 2** shows the experimental and theoretical XRD patterns of three compounds. The main peaks measured in the small-angle region ($<10^\circ$) closely match simulated peaks. In the wide-angle region ($>20^\circ$), peak intensities are weak; however, there is still good agreement between simulated and experimental peaks. Based on this comparison, it can be concluded that the majority of crystalline domains formed in the thin film state has similar molecular packing as those of the single crystals grown from solution. Therefore, detailed structural information from the single crystal structures of the studied compounds can be correlated to their solid-state properties.

Single crystal structures allow the determination of intermolecular packing in the solid state, which has been shown to influence optoelectronic properties. Typically, the intermolecular packing of conjugated molecules^[31] or polymers^[32,33] consists of layered structures in which their conjugated backbones overlap leading to π - π stacking. Therefore, comparison of intermolecular π - π interactions can be simplified by analyzing their layered structures. **Table 2** shows the unit cells,

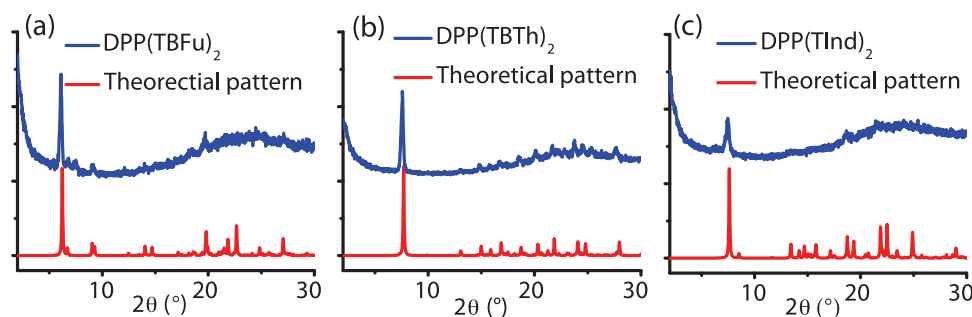
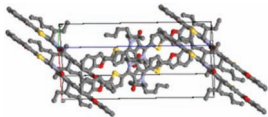
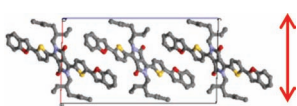
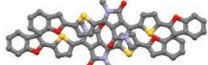
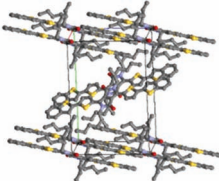
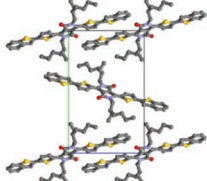
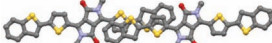
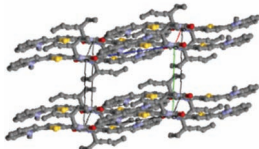
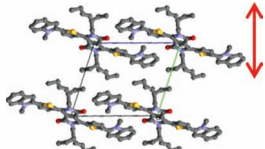
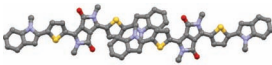


Figure 2. Experimentally measured XRD patterns of annealed thin films (top, in blue) and theoretical patterns (bottom, in red) simulated from single crystal structures of a) **DPP(TBFu)₂**, b) **DPP(TBTh)₂**, and c) **DPP(TInd)₂**.

Table 2. Summary of intermolecular packing of three dpp-containing compounds.

Compound	Side view ^{a)}	Layer structure ^{b)}	Intermolecular overlapping and distance ^{c)}
DPP(TBFu) ₂			 (3.32 Å)
DPP(TBTh) ₂			 (3.50 Å)
DPP(TInd) ₂			 (N/A) ^{d)}

^{a)}Unit cells viewed from side with C, O, N and S atoms shown in grey, red, cyan, and yellow, respectively. Only the mesomer of each compound is presented, and all hydrogen atoms were omitted for clarity. Unit cell axis *a*, *b*, and *c* are shown in red, green, and blue respectively; ^{b)}Viewed along unit axis (**DPP(TBFu)₂**: axis *b*; **DPP(TBTh)₂**: axis *a*; **DPP(TInd)₂**: axis *a*). Layer structures as indicated by red arrows are separated by alkyl chains with layer distance of 1.42 nm, 1.15 nm and 1.23 nm for **DPP(TBFu)₂**, **DPP(TBTh)₂**, and **DPP(TInd)₂**, respectively; ^{c)}Intermolecular packing inside the layer structures, viewed perpendicularly to the plane of conjugated backbones. Alkyl chains (2-ethylhexyl) are simplified as methyl groups for clarity. Distance value in parenthesis is calculated from distance of two parallel planes containing overlapping moieties; ^{d)} Not available due to twisted conformation at overlapping moieties.

layered structures separated by alkyl chains, and simplified intermolecular π - π stacking of the three compounds. Although these compounds have different intermolecular packing in unit cells, they exhibit layered structures which are well-separated by alkyl side chains with layer thicknesses ranging from 1.1 nm to 1.5 nm as indicated by red arrows.

As shown in Table 2, the π - π overlapping of **DPP(TBFu)₂** occurs on almost entire molecule, while that of **DPP(TBTh)₂** is only localized at the thiophene and benzothiophene moieties. **DPP(TInd)₂** overlaps only at the edge of the thiophene and *N*-methylindole moieties, where the twisted conformation (vide infra) between the moieties leads to inferior π orbital overlapping relative to the other compounds. The overlapping distances of **DPP(TBFu)₂** and **DPP(TBTh)₂** are determined from parallel planes containing the overlapping conjugated moieties. **DPP(TBTh)₂** has a larger overlapping distance than **DPP(TBFu)₂** (3.50 Å vs. 3.32 Å). This larger π - π distance results from the overlapping location of **DPP(TBTh)₂**, where the benzothiophenyl groups contain large sulfur atoms (Figure 1). The combination of large intermolecular interaction area and short π - π distance observed in **DPP(TBFu)₂** may lead to higher charge carrier mobility in the film state than that of **DPP(TBTh)₂**, as the similar packing between the single crystals and the films has been demonstrated by XRD pattern as shown in Figure 2.

It is noteworthy that the three compounds have completely different packing modes due to the different heteroatom substitution in end-conjugated units. In particular, **DPP(TBFu)₂** and **DPP(TBTh)₂** pack differently in the solid state even though the structural variation is limited to the difference between one O and S heteroatom in the indene ring. In the **DPP(TBFu)₂** unit cell, two adjacent oxygen atoms in benzofuranyl groups have an O-O distance of 3.087 Å as indicated in Figure 3a. Replacing the oxygen (van der Waals radius 1.52 Å) in the benzofuran moiety of **DPP(TBFu)₂** with sulfur leads to a strong repulsion between two sulfur atoms in adjacent molecules, due to the large van der Waals radius of sulfur (1.80 Å). This could be one primary reason that **DPP(TBTh)₂** cannot adopt the same packing mode

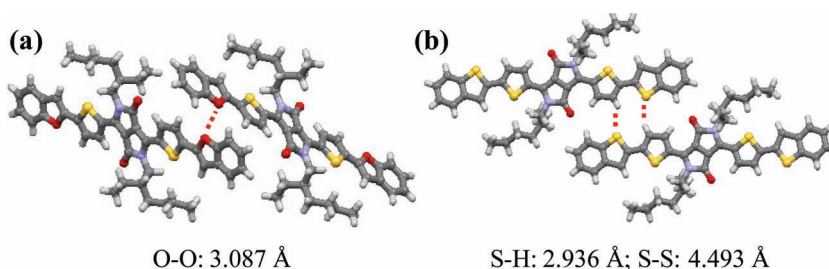
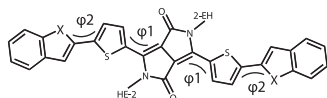


Figure 3. Two adjacent **DPP(TBFu)₂** (a) and **DPP(TBTh)₂** (b) molecules in their unit cells. The red dotted lines indicate intermolecular short contacts among the aromatic end-groups with the atom distance of O-O: 3.087 Å (a) and S-H: 2.936 Å (b). The S-S distance from adjacent aromatic end-groups in **DPP(TBTh)₂** is 4.493 Å. Van der Waals radii of O, S, and H are 1.52, 1.80, and 1.20 Å, respectively. C, O, N, and S atoms are shown in grey, red, cyan, and yellow, respectively.

Table 3. Conjugated backbone conformation of three dpp-containing molecules determined from single crystal structures.

Compound	$\phi 1^a$ [°]	$\phi 2^a$ [°]
DPP(TBFu) ₂	8.7	6.3
DPP(TBTh) ₂	5.5	3.2
DPP(TInd) ₂	14.1	34.9

^a) $\phi 1$ (C–C–C–C) and $\phi 2$ (X–C–C–C) as illustrated by the general molecular structure (below).



of DPP(TBFu)₂. Within the DPP(TBTh)₂ unit cell, the contacts between ending moieties in two molecules are S–H atoms with a distance of 2.936 Å as shown in Figure 3b. The S–S distance from adjacent aromatic end-groups is 4.493 Å, much larger than the corresponding O–O distance in the DPP(TBFu)₂ unit cell.

In addition to the intermolecular packing, molecular conformation is another type of structural information that can be obtained from single crystal structures. For each DPP-containing compound, molecules included in a unit cell have the same conformation. The conformation of the conjugated backbone can be described by the dihedral angles of σ bonds between conjugated moieties, i.e., $\phi 1$ and $\phi 2$ as displayed in Table 3. DPP(TBFu)₂ and DPP(TBTh)₂ have similar quasi-coplanar conformations, in which both $\phi 1$ and $\phi 2$ are less than 9°. In contrast, DPP(TInd)₂ exhibit a twisted conformation with larger $\phi 1$ and $\phi 2$ values (14.1° and 34.9°, respectively). The much larger $\phi 2$ in DPP(TInd)₂ is due to enhanced steric hindrance originating from the methyl substitution on the end-groups, which inhibit a coplanar conformation. In addition to backbone conformation, the alkyl chains (2-ethylhexyl) of three compounds have very similar conformation in which the long branch (butyl) extends along the molecular backbone plane and short branch (ethyl) extends out of the backbone plane.

The effects of heteroatom substitution on backbone conformation are also examined by DFT optimization at the B3LYP/6-31G* level in vacuo. The theoretical values of $\phi 1$ and $\phi 2$ calculated in this way compare well with the experimentally observed values. DPP(TBFu)₂ and DPP(TBTh)₂, which are predicted to have coplanar conformation ($\phi 1 = \phi 2 = 0^\circ$), exhibit a quasi-planar conformation ($\phi 1, \phi 2 < 9^\circ$) in the single crystals. For DPP(TInd)₂, the DFT calculation gives a $\phi 2$ of 34°, which is also very close to the experimental value (34.9°). Although the DFT calculations model the molecules in vacuo without considering the intermolecular interactions, they nonetheless provide a useful approach to evaluate the effect of heteroatom substitution on conformation. Conjugated molecules that have a planar conformation predicated by DFT calculation often possess a quasi-planar conformation in the solid state.

Because the conformation is an elementary aspect of intermolecular interactions in solid state, it is correlated with many material's properties such as solid-state intermolecular packing, thermal properties, and solubility. The twisted conformation observed in DPP(TInd)₂ significantly reduces the intermolecular

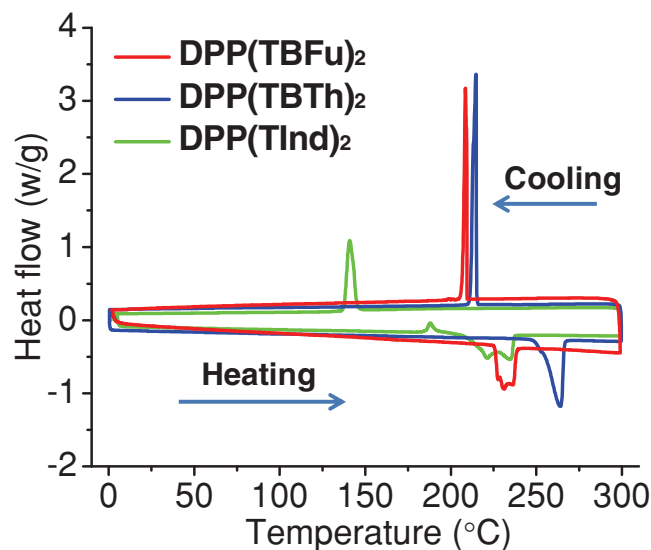


Figure 4. DSC curves of DPP(TBFu)₂, DPP(TBTh)₂, and DPP(TInd)₂ determined with a scanning rate of 5 °C/min under N₂.

π – π overlapping as shown in Table 2. For conjugated molecules, the intermolecular interaction is dominated by π – π interaction. Therefore, DPP(TInd)₂ is expected to have lower thermal transition temperatures, low crystallinity, and high solubility (vide infra).

2.2. Thermal Properties, Solubility, and Film Morphology

In most optoelectronic devices, the device performance is significantly related to the film formation ability of conjugated molecules, which is affected by materials' physical properties such as thermal properties, solubility, and film morphology.

Figure 4 shows the differential scanning calorimetry (DSC) thermograms of three DPP-containing compounds. The phase transition temperatures including melting temperature (T_m) and crystallization temperature (T_c) are listed in Table 4. Both T_m and T_c have a sequence of DPP(TBTh)₂ > DPP(TBFu)₂ > DPP(TInd)₂. All three compounds have T_c higher than 210 °C.

DPP(TBTh)₂ and DPP(TBFu)₂ exhibit sharp crystallization peaks at high temperature (>200 °C) indicating good crystallization ability. In contrast, DPP(TInd)₂ exhibits a small crystallization peak at 145 °C and a cold crystallization peak at 190 °C, which are typically correlated to a low crystallization ability. Such effects on thermal transitions are attributed to differences in intermolecular interactions arising from the heteroatom substitution. As revealed by single crystal structures, the twisted conformation of DPP(TInd)₂ reduces the primary intermolecular interaction of conjugated molecules, e.g., π – π interaction, resulting in a low T_m as well as inferior crystallization ability. DPP(TBTh)₂ has a higher T_m than DPP(TBFu)₂ which may be ascribed to the enhanced intermolecular interactions resulted from the heavier heteroatoms (S atom) in the aromatic end-groups.

The difference in phase transition temperatures due to heteroatom substitutions indicates the varying strength of

Table 4. Thermal properties, solubility, optical absorption, and frontier orbitals of three dpp derivatives.

Compound	Thermal Properties			Solubility ^{c)} [mg/mL]	Optical absorption ^{d)}		Frontier orbitals	
	T_m ^{a)} [°C]	T_c ^{a)} [°C]	T_d ^{b)} [°C]		λ_{onset} [nm]	Bandgap ^{e)} [eV]	HOMO ^{f)} [eV]	LUMO ^{g)} [eV]
DPP(TBFu) ₂	226	209	403	15	709	1.75	−5.14	−3.39
DPP(TBTh) ₂	254	212	402	<4	721	1.72	−5.19	−3.47
DPP(TInd) ₂	214	145	402	32	712	1.74	−5.07	−3.33

^{a)}Melting point on heating scan by DSC under N₂; ^{b)}Temperature with 5% weight loss by TGA under N₂; ^{c)}In chloroform at room temperature, determined by the method in ref. [33]; ^{d)}Determined from the film absorption in Figure 6b; ^{e)}Solid-state optical bandgap calculated from $E_g^{\text{opt}} = 1240/\lambda_{\text{onset}}$ in the absorption spectrum; ^{f)}Measured by UPS; ^{g)}Calculated by LUMO = $E_g^{\text{opt}} - |\text{HOMO}|$.

intermolecular interactions, which is related material's properties such as crystallinity and solubility. Empirically, for a series of compounds with similar structures, compounds with higher T_m typically have higher crystallinity and lower solubility. The solubilities of the three compounds were determined in chloroform at room temperature by a reported method^[34] and are listed in Table 4. Three compounds have a solubility sequence of DPP(TBTh)₂ < DPP(TBFu)₂ < DPP(TInd)₂, opposite to the sequence of melting temperatures. DPP(TInd)₂ has the highest solubility (32 mg/mL in chloroform) due to weak π - π interactions resulting from a twisted conformation and the additional two methyl groups on the N atoms of the ending heterocycles as observed from the single crystal structure. DPP(TBFu)₂ has higher solubility than DPP(TBTh)₂ (15 mg/mL vs. <4 mg/mL) because of stronger van der Waals interaction in DPP(TBTh)₂ as indicated by its higher T_m .

The thermal stability of these compounds was investigated by thermal gravimetric analysis (TGA) at a heating rate of 10 °C/min under N₂. Table 4 lists 5% weight loss temperatures (T_d) of these compounds determined from TGA curves (Figure S2, Supporting Information). Each compound exhibits excellent thermal stability with a T_d of approximately 400 °C, similar to other reported DPP-containing conjugated materials.^[35–37]

The morphology of as-cast and annealed neat films of three DPP-containing compounds spun from chloroform was

investigated by atomic force microscopy (AFM). The films were annealed at 100 °C for 10 min in nitrogen environment. As shown in Figure 5, the as-cast films exhibit small domains with the surface roughness of 0.7 nm for DPP(TBFu)₂, 0.9 nm for DPP(TBTh)₂, and 2.0 nm for DPP(TInd)₂. After thermal annealing, the surface morphology changes significantly. DPP(TBTh)₂ and DPP(TInd)₂ films display large crystalline domains embedded within layer structures whereas DPP(TBFu)₂ film shows fibril-like morphology. Further annealing at a higher temperature (125 °C) leads to larger crystalline domains in the films of DPP(TBFu)₂ and DPP(TBTh)₂ (Figure S3, Supporting Information). The surface morphology of DPP(TInd)₂ does not change significantly. The DPP(TBTh)₂ film shows only large crystalline domains up to 500 nm by 500 nm. The tendency of DPP(TBTh)₂ to form crystalline domains in thin film agrees well with DSC result that DPP(TBTh)₂ has a higher T_m . The observed crystalline domain morphology of these compounds in thin films is comparable to the corresponding morphology of their single crystals (Figure S1, Supporting Information). This similarity in the morphology for each compound agrees well with the similar molecular stacking between the single crystal and the film state, as confirmed by XRD patterns in Figure 2. Therefore, the effect of heteroatom substitutions on film morphology largely originates from their influence on crystal structures and molecular packing.

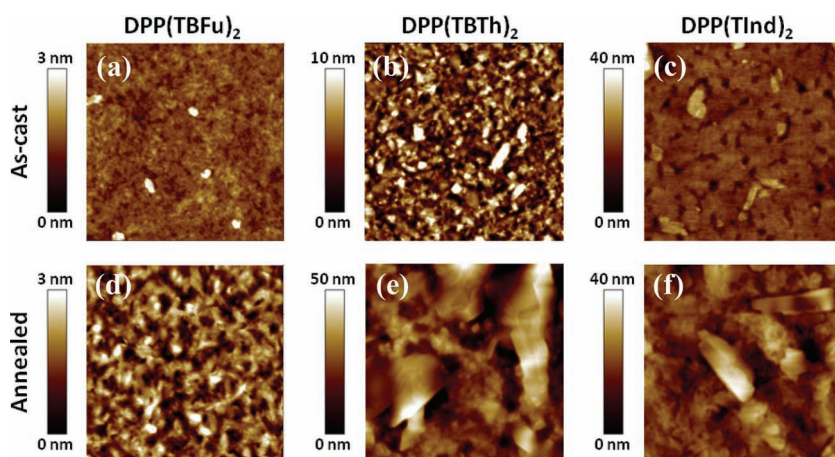


Figure 5. As-cast (top: a–c) and annealed (bottom: d–f) AFM topographic images of DPP(TBFu)₂ (a,d), DPP(TBTh)₂ (b,e), and DPP(TInd)₂ (c,f). Annealing conditions: 100 °C for 10 min. Scan size: 1 $\mu\text{m} \times 1 \mu\text{m}$.

2.3. Optical Absorption and Frontier Orbital Levels

The optical absorption in both solution and solid state were measured to examine the effects of heteroatom substitutions. Figure 6a displays the UV-vis absorption spectra of these compounds in chloroform composed of three primary absorption bands in the ranges of approximately 320–370 nm, 390–450 nm, and 500–670 nm. The strongest absorption band at 500–670 nm is ascribed to the intramolecular charge transfer (ICT) band generated by DPP and thienyl moieties. The other absorption bands can be resulted from π - π^* transitions of the ending heterocycles and their conjugations with thienyl moieties. DPP(TBFu)₂ and DPP(TBTh)₂ have

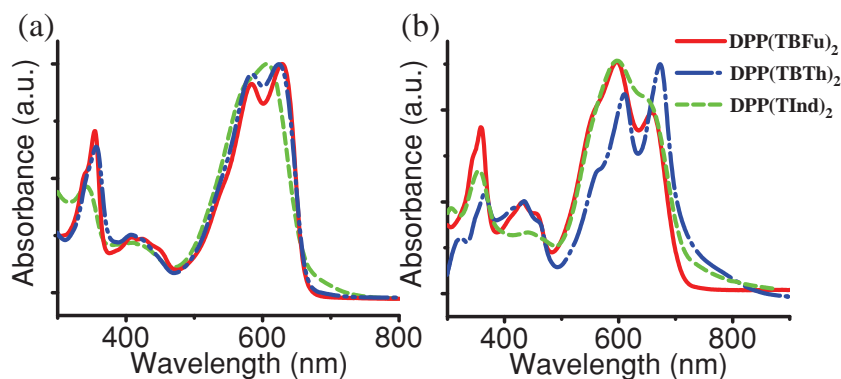


Figure 6. UV-Vis absorption in chloroform (a) and as-cast film (b) of three DPP-containing compounds (**DPP(TBFu)₂**: solid red curve; **DPP(TBTh)₂**: dash-dotted blue curve; and **DPP(TInd)₂**: dashed line green curve).

very similar solution absorption profiles with the wavelength of maxima absorption (λ_{max}) at 624 and 628 nm, respectively. **DPP(TInd)₂** exhibits a blueshift on λ_{max} (607 nm) compared with other two compounds, which can be ascribed to its favored nonplanar conformation revealed by both single crystal structure and DFT optimization.

Compared to the absorption in solution, the charge transfer band of the as-cast (Figure 6b) and annealed (Figure S4, Supporting Information) film of three compounds is broadened and significantly red-shifted. Each compound exhibits two vibronic peaks: 597 and 658 nm for **DPP(TBFu)₂**, 612 and 676 nm for **DPP(TBTh)₂**, and 595 and 648 nm for **DPP(TInd)₂**. The solid-state optical absorption of conjugated materials is primarily determined by conformation and molecular packing.^[38–40] **DPP(TBFu)₂** and **DPP(TInd)₂** have similar absorption profiles as well as the position of vibronic peaks. In contrast, **DPP(TBTh)₂** exhibits a sharp and red-shifted (≈ 20 nm) vibronic peaks mainly attributed to different intermolecular packing as revealed by single crystal structures and higher degree of crystallinity in films as compared to that of **DPP(TBFu)₂**. **DPP(TInd)₂** exhibits a similar absorption as **DPP(TBFu)₂** although **DPP(TInd)₂** has a twisted conformation in solid state. The twisted conformation of **DPP(TInd)₂** seems not to reduce the conjugation length significantly. Such similar effect is also observed in other conjugated molecules in which the dihedral angles along the conjugated backbones are less than 20° .^[35,41]

Using the onset of optical absorption (λ_{onset}), optical bandgaps of three DPP films are calculated and listed in Table 4. Three compounds have very similar optical bandgaps ranging from 1.72 to 1.75 eV. Frontier energy levels such as the highest occupied molecular orbital (HOMO) and the lowest unoccupied molecular orbital (LUMO) determined from ultraviolet photoelectron spectroscopy (UPS) measurements (Figure S5, Supporting Information) are also listed in Table 4. The frontier energy levels of these DPP-containing compounds are similar with HOMO and LUMO levels approximately at -5.1 eV and -3.4 eV, respectively.

Overall, changing the heteroatom substitution in the end-groups does not affect the optical absorption, bandgap, and frontier orbital levels significantly. Similar results were also observed in other molecular architectures such as pyridal[2,1,3]

thiadiazole-containing conjugated molecules.^[42] One possible reason for this insensitive dependence of optical properties as revealed by DFT is that end-groups have less contribution on the HOMO and LUMO orbitals (Figure S6, Supporting Information). Most HOMO and LUMO orbitals are located on the central DPP and adjacent thienyl rings.

2.4. Hole Mobility

Hole-only diodes and field effect transistors (FETs) were fabricated from thin films of each material to measure the hole mobilities in both perpendicular to and in the plane of the film, respectively. The details of device

architectures, current density–voltage (J – V) characteristics of hole-only diodes and output characterization of FETs are shown in Figures S7 and S8 (Supporting Information). The hole mobilities of as-cast and annealed films are summarized in Table 5.

For the hole-only diodes, the extracted hole mobility using space charge limited current (SCLC) model of as-cast **DPP(TBFu)₂** film is $3.6 \times 10^{-6} \text{ cm}^2/\text{Vs}$. After a thermal annealing, the hole mobility is increased to $9.0 \times 10^{-5} \text{ cm}^2/\text{Vs}$. This result agrees well with AFM and thin film XRD results that thermal annealing leads to higher degree of crystallinity. Compared with that of **DPP(TBFu)₂**, the hole mobility of **DPP(TInd)₂** is considerably small. Prior to annealing, the hole mobility is found to be $3.0 \times 10^{-7} \text{ cm}^2/\text{Vs}$, and increases to $2.0 \times 10^{-6} \text{ cm}^2/\text{Vs}$ after annealing at 100°C . Hole-only diodes prepared from **DPP(TBTh)₂** do not exhibit a SCLC, instead, the current is ohmic and has a linear dependence on applied bias over a large voltage range, resembling a short-circuit. These characteristics may be due to films of the material being relatively thin (less than 80 nm due to the limited solubility as shown in Table 4), as well as being fairly rough, leading to the majority of the current concentrating in and passing through localized areas where the film is especially thin.^[43]

The hole mobility determined from FETs was extracted from the slope of the transfer curves in the saturation regime. As-cast films of **DPP(TBFu)₂** exhibit a hole mobility of $6.4 \times 10^{-6} \text{ cm}^2/\text{Vs}$, thermal annealing increase the hole mobility to $5.3 \times 10^{-4} \text{ cm}^2/\text{Vs}$.

Table 5. Hole mobility of three DPP-containing compounds measured by hole-only diodes and FETs.

Compound	Hole Mobility (cm^2/Vs)			
	Hole-only diode ^{a)}		FET ^{c)}	
	As cast	Annealed ^{d)}	As cast	Annealed ^{d)}
DPP(TBFu)₂	2.2×10^{-6}	1.5×10^{-5}	6.4×10^{-6}	5.3×10^{-4}
DPP(TBTh)₂	NA ^{b)}	NA ^{b)}	2.6×10^{-6}	4.3×10^{-5}
DPP(TInd)₂	3.0×10^{-7}	2.0×10^{-6}	7.7×10^{-7}	1.5×10^{-5}

^{a)}Space charge limited current (SCLC) mobility measured from neat films; ^{b)}No SCLC measured; ^{c)}Field effect transistor with bottom-gate and top-contact configuration; ^{d)}Conditions for annealing: 100°C for 10 min.

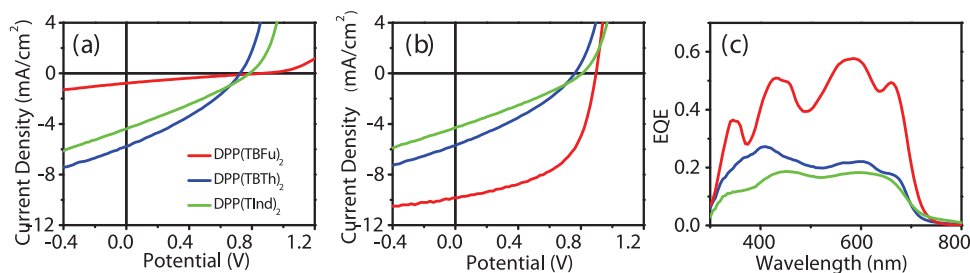


Figure 7. J - V characteristics of as-cast devices (a) and optimized devices (b) by thermal annealing under 100 mW/cm² simulated solar illumination, and EQE spectra (c) of optimized devices.

Vs. This increase in mobility upon thermal annealing is similar to the observation for vertical charge transport measured by hole-only diodes. **DPP(TBTh)₂** has the field-effect mobility of 2.6×10^{-6} cm²/Vs for as-cast films and increases to 4.3×10^{-5} cm²/Vs upon thermal annealing. **DPP(TInd)₂** shows hole mobilities of 7.7×10^{-7} and 1.5×10^{-5} cm²/Vs, for as-cast and annealed devices, respectively. As demonstrated by AFM morphology in Figure 5, annealing leads to enhanced film crystallinity, which is manifested in increased field-effect hole mobilities after thermal annealing.

The carrier mobilities of bulk films measured by both hole-only diodes and FETs exhibit a similar trend among these DPP-conjugated materials. **DPP(TBFu)₂** exhibits the highest hole mobility for both as-cast and annealed films while **DPP(TInd)₂** shows the lowest mobilities. The difference in hole mobility observed for **DPP(TBFu)₂** and **DPP(TInd)₂** can most likely be ascribed to differences in molecular packing. **DPP(TBFu)₂** has much stronger π - π overlapping (larger overlapping area) and shorter intermolecular distance than those of **DPP(TInd)₂**, which should result in higher carrier mobility. The results indicate a correlation within this class of materials that compounds with better intermolecular overlapping in single crystal structures have better carrier transportation in polycrystalline films.

2.5. Solar Cell Performance

Solar cell devices were prepared from blends of each donor material with phenyl-C₇₁-butyric acid methyl ester (PC₇₁BM) as the electron acceptor, and optimized with respect to donor-acceptor blend ratio and annealing temperature. Typical J - V curves of optimized devices and the corresponding as-cast devices under one sun illumination (AM 1.5, 100 mW cm⁻²)

are displayed in Figure 7a,b. The external quantum efficiency (EQE) spectra of optimized devices are displayed in Figure 7c. All device characteristics are summarized in Table 6.

The optimal device of **DPP(TBTh)₂** was produced by the 50:50 donor-acceptor ratio after annealing at a moderate temperature of 80 °C, giving a short circuit current (J_{SC}) of 5.70 mA/cm², open-circuit voltage (V_{OC}) of 0.76 V, fill factor (FF) of 0.33 and power conversion efficiency (PCE) of 1.43%. The **DPP(TInd)₂** device with the highest performance was obtained with an acceptor-rich blend (30:70) after annealing at the same temperature (80 °C), producing a J_{SC} of 4.31 mA/cm², V_{OC} of 0.81 V, FF of 0.30 and PCE of 1.03%. Annealing at higher temperatures of both **DPP(TBTh)₂** and **DPP(TInd)₂** devices results in a significant decrease of device performances. Compared with the as-cast devices, thermal annealing only slightly improves device performance. In contrast, the device performance of **DPP(TBFu)₂** is significantly enhanced by thermal annealing; the PCE increases from 0.15% to 4.8% after annealing at 110 °C. The higher PCE is a result of improved J_{SC} (0.78 mA/cm² vs. 9.85 mA/cm²) and FF (0.22 vs. 0.54). All the external quantum efficiency (EQE) spectra as shown in Figure 7c have onsets in the range of 710–720 nm, consistent with the onsets of the broad absorption bands observed for all three materials and the magnitude of each spectrum correlate with the observed J_{SC} 's. **DPP(TBFu)₂** exhibits much higher quantum efficiency than other two compounds, which correlates well to its excellent performance.

The AFM topographic and phase images of active layers in the optimized solar cell devices are shown in Figure 8. The blend film of **DPP(TBFu)₂**:PC₇₁BM has a similar fibril-like morphology as **DPP(TBFu)₂** neat film. This ability of **DPP(TBFu)₂** to form nanoscale fiber-like networks after thermal annealing (Figure 8d) facilitates the formation of

Table 6. Summary of solar cell device characteristics of each material with PC₇₁BM under AM 1.5G, 100 mW cm⁻² illumination.

Compound	Ratio	Annealing	J_{SC}	V_{OC} [V]	FF	PCE [%]
DPP(TBTh)₂	50:50	As-cast	5.77	0.73	0.33	1.36
	50:50	80 °C	5.70	0.76	0.33	1.43
DPP(TInd)₂	30:70	As-cast	4.40	0.79	0.29	0.99
	30:70	80 °C	4.31	0.81	0.30	1.03
DPP(TBFu)₂	60:40	As-cast	0.78	0.87	0.22	0.15
	60:40	110 °C	9.85	0.90	0.54	4.80

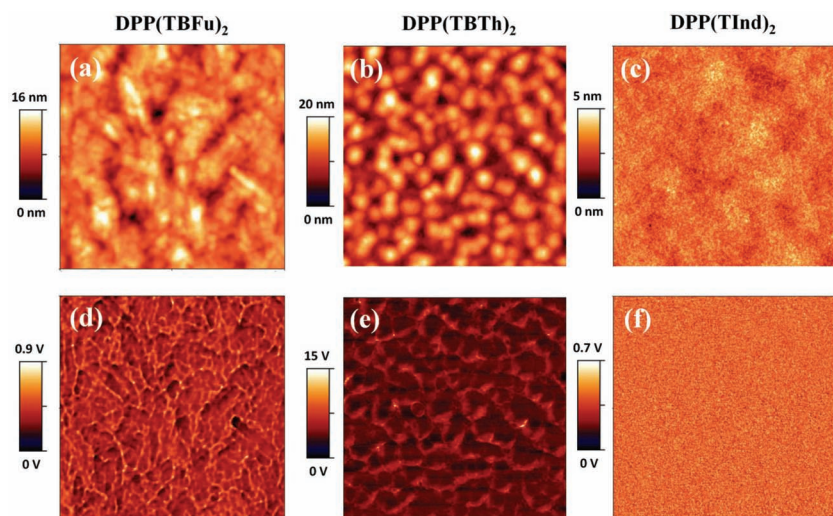


Figure 8. AFM topographic (top: a–c) and phase (bottom: d–f) images of **DPP(TBFu)₂**:PC₇₁BM (a,d), **DPP(TBTh)₂**:PC₇₁BM (b,e), and **DPP(TInd)₂**:PC₇₁BM (c,f) collected from optimized solar cells. Scan size: 2 $\mu\text{m} \times 2 \mu\text{m}$.

desirable phase separation for BHJ,^[7] which is likely the primary reason for its superior device performance. In contrast, the **DPP(TBTh)₂**:PC₇₁BM film shows granular morphology indicating larger phase separation, possibly due to lower solubility of **DPP(TBTh)₂**. The **DPP(TInd)₂**:PC₇₁BM is very smooth with no phase contrast (Figure 8c,f). The large difference in the magnitude of the EQE for **DPP(TBFu)₂** can likely be attributed to its more optimal phase separated morphology with PC₇₁BM as well as greater charge carrier mobility, which allows much more efficient extraction of photo-generated charge carriers.

It can be observed that device characteristics correlate well with the each materials' thus presented properties. Although their molecular structures and optical properties are very similar, differences in the heteroatom substitution of each material has a profound effect on solubility, the capability of film formation, charge carrier mobility and phase separation with PC₇₁BM, which in turn affects their performance in BHJ solar cells.

3. Conclusions

In summary, the effects of heteroatom substitutions on the properties of conjugated molecules have been evaluated by comparing three DPP-containing compounds with different aromatic heterocycles as end-groups. Single crystal structures of the three compounds reveal that the heteroatom substitutions in end-conjugated units have a significant impact on both intramolecular and intermolecular interactions, which subsequently affect materials' various solid-state properties such as film formation and charge carrier mobility, and thereby influencing the performance of electric devices. In addition, the effect of heteroatom substitutions on conformation and optical absorption can be qualitatively evaluated via DFT computation. Our investigation demonstrates that single crystal structures are a useful platform to understand structure-property relationships in conjugated small molecules. Within this series,

DPP(TBTh)₂ having low solubility and high tendency to crystallize forms large phase separation when blended with PC₇₁BM and low performance. **DPP(TInd)₂** has high solubility and blends too well with PC₇₁BM in conjunction with having low mobility resulting in low performance. **DPP(TBFu)₂** has a moderate solubility and better film morphology in the blend leading to highest PCE among the three DPP derivatives. The utility of conjugated small molecules to elucidate structure-property relationships are of vital importance in understanding how chemical structures develop into the material properties associated with the thin films used in organic electronic devices. Insight into such relationships will be beneficial for the design of new conjugated molecules for use in organic solar cells as well as other functional applications.

4. Experimental Section

Materials: Benzothiophen-2-boronic acid was purchased from Frontier Scientific. N-Methylindole-2-tributylstannane was purchased from Synthonix and used as received. Tris(dibenzylideneacetone) dipalladium, tetrakis(triphenylphosphine)palladium and other reagents were purchased from Sigma Aldrich and used as received. Toluene was dried over sodium/benzophenone, distilled at reduced pressure. Chloroform, tetrahydrofuran, and other solvents were used without any further purification. Flash chromatography was performed using Silicyle SiliaFlash P60 (particle size 40–63 μm , 230–400 mesh) silica gel.

Characterization: UV-vis absorption spectroscopy was measured on a Shimadzu 2401 diode array spectrometer. All solution UV-Vis measurements were run in CHCl₃. Film samples were prepared by spin-coating CHCl₃ solutions onto quartz substrates. ¹H and ¹³C nuclear magnetic resonance (NMR) spectroscopy spectra were recorded with a 400 MHz spectrometer (Varian, ASM-100) at 25 °C using CDCl₃ as a solvent. Field desorption mass spectroscopy was carried out on a Waters GCT Premier high resolution time-of-flight mass spectrometer equipped with a field ionization/field desorption (FI/FD) ion sources. DSC was determined under N₂ using a TA Instrument (Model Q-20) at a rate of 10 °C/min in a temperature range of 0–300 °C. To remove the effect of thermal history, the third heating and cooling scan loop was employed to determine thermal transition temperatures. AFM images were collected in air under ambient conditions using the Innova scanning probe microscope (Veeco). Silicon probes with resonant frequencies of 75 KHz (Budget Sensors) were used for tapping mode AFM measurements. UPS was carried out using He I ($h\nu = 21.2 \text{ eV}$) source equipped with hemispherical electron energy analyzer (Kratos Ultra Spectrometer). Film samples for UPS measurement were prepared by spin coating of a small molecule solution (2 mg/mL in chloroform) at 3000 rpm onto thermally deposited Au films (75 nm) on Si substrates. All samples were prepared in a N₂ atmosphere glovebox and were transferred via an airtight sample holder to the UPS analysis chamber. To gain strong diffraction singles, powder samples that were scratched from thin films were used to evaluate film X-ray diffractions. The thin films were cast from chloroform solutions and annealed at 100 °C for 10 min. The X-ray diffractions were recorded on a Bruker D8 diffractometer with Cu K α radiation ($\lambda = 1.54178 \text{ \AA}$).

Crystallography: Single crystal X-ray diffraction was collected on a Bruker Kappa Apex II diffractometer using a graphite monochromator with a Mo K α X-ray source ($\lambda = 0.71073 \text{ \AA}$). The crystals were mounted

on a nylon loop under Paratone-N oil, and all data were collected at 100 K using an Oxford nitrogen gas cryostream system. Data collection, cell parameter determination, data integration, and parameter refinement were performed using Apex2 software (V2011). Absorption correction of the data was applied using SADABS software. Structure determination was done using direct method and difference Fourier techniques. All hydrogen atom positions were idealized and rode on the atom of attachment. Structure solution and refinement were performed using SHELXTL. Crystallographic data for the structures reported in this paper have been deposited with the Cambridge Crystallographic Data Centre and allocated the deposition numbers of CCDC 866382–866384.

Theoretical Calculation: All calculations were examined using the Gaussian03 program package. Density functional theory at the B3LYP/6-31G* level in vacuo was applied to optimize the ground-state geometries of the considered molecules in the gas phase.

Device Fabrication: Solar cells were fabricated by spin-casting the BHJ active layer onto a approximate 50 nm layer of PEDOT:PSS (H.C. Stark Baytron P4083) atop Corning 1737 glass patterned with 140 nm of indium tin oxide (ITO). The ITO glass substrate was first cleaned with detergent, ultrasonicated in acetone and isopropyl alcohol, and dried overnight in an oven. PEDOT:PSS layer was dried for 10 min at 140 °C in air and then transferred into a glovebox to spin-cast the BHJ layer. The BHJ layer was spin-cast from a solution consisting of a mixture of DPP-containing molecule and PC₇₁BM in chloroform. The active layer thicknesses were determined using an Ambios XP-100 Stylus profilometer. Solar cells were characterized under simulated 100 mW/cm² AM1.5G irradiation from a 300 W Xe arc lamp with an AM1.5 global filter. Simulator irradiance was characterized using a calibrated spectrometer, and illumination intensity was set using an NREL certified silicon diode with an integrated KG1 optical filter; spectral mismatch factors were calculated to be less than 10%. Quantum efficiencies were measured with a Xe lamp, monochromator, optical chopper, and lock-in amplifier; photon flux was determined by a calibrated silicon photodiode. Device fabrication and testing were done under inert atmosphere in a nitrogen filled glove box.

Hole-only diodes were fabricated using a architecture of ITO/PEDOT:PSS/[DPP derivative]/Au. Mobilities were extracted by fitting the current density–voltage curves using the Mott-Gurney relationship (space-charge-limited-current model, SCLC). FET devices were fabricated by spin casting thin layers of each material atop Si substrates with a native dielectric layer of SiO₂ using gold source and drain contacts (top-contact, channel width = 20 μm). Hole mobilities were extracted from the slope of the transfer curve in the saturation regime.

Supporting Information

Supporting Information is available from the Wiley Online Library or from the author.

Acknowledgements

J.L. and B.W. contributed equally to this work. The authors thank the National Science Foundation SOLAR (DMR-1035480) for supporting the synthesis and characterization of the materials and device evaluation. Single crystal and conformational studies were supported by the National Science Foundation American Competitiveness and Innovation Fellowship (DMR-1035480). T.Q.N. thanks the Camille Dreyfus Teacher Scholar Award and the Alfred Sloan Research Fellowship program. The authors acknowledge the California NanoSystems Institute at UCSB for computational resources. The authors thank Prof. Junghwa Seo for performing UPS experiments.

Received: June 13, 2012

Published online: August 9, 2012

- [1] J. Roncali, *Acc. Chem. Res.* **2009**, 42, 1719.
- [2] Y. Li, Q. Guo, Z. Li, J. Pei, W. Tian, *Energy Environ. Sci.* **2010**, 3, 1427.
- [3] B. Walker, C. Kim, T.-Q. Nguyen, *Chem. Mater.* **2010**, 23, 470.
- [4] A. Mishra, P. Bäuerle, *Angew. Chem. Int. Ed.* **2012**, 51, 2020.
- [5] Y. Sun, G. C. Welch, W. L. Leong, C. J. Takacs, G. C. Bazan, A. J. Heeger, *Nat. Mater.* **2012**, 11, 44.
- [6] Y. Matsuo, Y. Sato, T. Niinomi, I. Soga, H. Tanaka, E. Nakamura, *J. Am. Chem. Soc.* **2009**, 131, 16048.
- [7] B. Walker, A. B. Tamayo, X. D. Dang, P. Zalar, J. H. Seo, A. Garcia, M. Tantiwiwat, T.-Q. Nguyen, *Adv. Funct. Mater.* **2009**, 19, 3063.
- [8] A. B. Tamayo, B. Walker, T.-Q. Nguyen, *J. Phys. Chem. C* **2008**, 2, 11545.
- [9] A. B. Tamayo, X.-D. Dang, B. Walker, J. H. Seo, T. Kent, T.-Q. Nguyen, *Appl. Phys. Lett.* **2009**, 94, 103301.
- [10] O. P. Lee, A. T. Yiu, P. M. Beaujuge, C. H. Woo, T. W. Holcombe, J. E. Millstone, J. D. Douglas, M. S. Chen, J. M. J. Fréchet, *Adv. Mater.* **2011**, 23, 5359.
- [11] S. Loser, C. J. Bruns, H. Miyauchi, R. P. Ortiz, A. Facchetti, S. I. Stupp, T. J. Marks, *J. Am. Chem. Soc.* **2011**, 133, 8142.
- [12] J. Mei, K. R. Graham, R. Stalder, J. R. Reynolds, *Org. Lett.* **2010**, 12, 660.
- [13] K. R. Graham, J. Mei, R. Stalder, J. W. Shim, H. Cheun, F. Steffy, F. So, B. Kippelen, J. R. Reynolds, *ACS Appl. Mater. Interfaces* **2011**, 3, 1210.
- [14] F. Silvestri, M. D. Irwin, L. Beverina, A. Facchetti, G. A. Pagani, T. J. Marks, *J. Am. Chem. Soc.* **2008**, 130, 17640.
- [15] D. Bagnis, L. Beverina, H. Huang, F. Silvestri, Y. Yao, H. Yan, G. A. Pagani, T. J. Marks, A. Facchetti, *J. Am. Chem. Soc.* **2010**, 132, 4074.
- [16] U. Mayerhoffer, K. Deing, K. Größ, H. Braunschweig, K. Meerholz, F. Würthner, *Angew. Chem. Int. Ed.* **2009**, 8776.
- [17] G. Wei, S. Wang, K. Renshaw, M. E. Thompson, S. R. Forrest, *ACS Nano* **2010**, 4, 1927.
- [18] G. Wei, S. Wang, K. Sun, M. E. Thompson, S. R. Forrest, *Adv. Energy Mater.* **2011**, 1, 184.
- [19] F. Lincker, B. Heinrich, R. De Bettignies, P. Rannou, J. Pécaut, B. Grévin, A. Pron, B. Donnio, R. Demadrille, *J. Mater. Chem.* **2011**, 21, 5238.
- [20] B. Yin, L. Yang, Y. Liu, Y. Chen, Q. Qi, F. Zhang, S. Yin, *Appl. Phys. Lett.* **2010**, 97, 023303.
- [21] Y. Liu, X. Wan, F. Wang, J. Zhou, G. Long, J. Tian, J. You, Y. Yang, Y. Chen, *Adv. Energy Mater.* **2011**, 1, 771.
- [22] Z. Li, G. He, X. Wan, Y. Liu, J. Zhou, G. Long, Y. Zuo, M. Zhang, Y. Chen, *Adv. Energy Mater.* **2012**, 2, 74.
- [23] D. Demeter, T. Rousseau, P. Leriche, T. Cauchy, R. Po, J. Roncali, *Adv. Funct. Mater.* **2011**, 21, 4379.
- [24] T. Rousseau, A. Cravino, T. Bura, G. Ulrich, R. Ziessel, J. Roncali, *J. Mater. Chem.* **2009**, 19, 2298.
- [25] T. Rousseau, A. Cravino, E. Ripaud, P. Leriche, S. Rihn, A. De Nicola, R. Ziessel, J. Roncali, *Chem. Commun.* **2010**, 46, 5082.
- [26] N. M. Kronenberg, M. Deppisch, F. Würthner, H. W. A. Lademann, K. Deing, K. Meerholz, *Chem. Commun.* **2008**, 6489.
- [27] H. Bürckstümmer, N. M. Kronenberg, M. Gsänger, M. Stolte, K. Meerholz, F. Würthner, *J. Mater. Chem.* **2010**, 20, 240.
- [28] H. Bürckstümmer, E. V. Tulyakova, M. Deppisch, M. R. Lenze, N. M. Kronenberg, M. Gsänger, M. Stolte, K. Meerholz, F. Würthner, *Angew. Chem. Int. Ed.* **2011**, 50, 11628.
- [29] E. Ripaud, D. Demeter, T. Rousseau, E. Boucard-Céto, M. Allain, R. Po, P. Leriche, J. Roncali, *Dyes Pigments* **2012**, 95, 126.
- [30] Due to the chiral 2-ethylhexyl side chains, each as-synthesized compounds has three stereoisomers. The single crystals of **DPP(TBth)₂** and **DPP(TInd)₂** are obtained using as-synthesized isomer mixtures;

the single crystal of **DPP(TBFu)₂** was obtained using its mesomer. The stereoisomer effects on DPP-containing molecules will be published elsewhere.

- [31] M. D. Curtis, J. Cao, J. W. Kampf, *J. Am. Chem. Soc.* **2004**, *126*, 4318.
- [32] J. Liu, M. Arif, J. Zou, S. I. Khondaker, L. Zhai, *Macromolecules* **2009**, *42*, 9390.
- [33] J. Liu, I. A. Mikhaylov, J. Zou, I. Osaka, A. E. Masunov, R. D. McCullough, L. Zhai, *Polymer* **2011**, *52*, 2302.
- [34] B. Walker, A. Tamayo, D. T. Duong, X. Dang, C. Kim, J. Granstrom, T.-Q. Nguyen, *Adv. Energy Mater.* **2011**, *1*, 221.
- [35] C. Kim, J. Liu, J. Lin, A. B. Tamayo, B. Walker, G. Wu, T.-Q. Nguyen, *Chem. Mater.* **2012**, *24*, 1699.
- [36] J. David, M. Weiter, M. Vala, J. Vyřuchal, J. Kučerík, *Dyes Pigments* **2011**, *89*, 137.
- [37] P. Sonar, G. Ng, T. T. Lin, A. Dodabalapur, Z. Chen, *J. Mater. Chem.* **2010**, *20*, 3632.
- [38] J. Mizuguchi, *J. Phys. Chem. A* **2000**, *104*, 1817.
- [39] S. Varghese, S. Das, *J. Phys. Chem. Lett.* **2011**, *2*, 863.
- [40] A. B. Koren, M. D. Curtis, A. H. Francis, J. W. Kampf, *J. Am. Chem. Soc.* **2003**, *125*, 5040.
- [41] G. Klaerner, R. D. Miller, *Macromolecules* **1998**, *31*, 2007.
- [42] Z. B. Henson, G. C. Welch, T. van der Poll, G. C. Bazan, *J. Am. Chem. Soc.* **2012**, *134*, 3766.
- [43] N. Koch, A. Elschner, J. Schwartz, A. Kahn, *Appl. Phys. Lett.* **2003**, *82*, 2281.